journal of
MOLECULAR
LIQUIDS

Journal of Molecular Liquids 368 (2022) 120659

Contents lists available at ScienceDirect

Journal of Molecular Liquids

journal homepage: www.elsevier.com/locate/molliq

On the structure of cetylpyridinium perchlorate: A combined XRD, NMR, IR and DFT study

Oksana Fizer [a,b], Maksym Fizer [a,*], Michael Filep [c,d], Vasyl Sidey [e], Ruslan Mariychuk [f]

[a] Department of Organic Chemistry, Educational and Scientific Institute of Chemistry and Ecology, Uzhhorod National University, Pidhirna 46, Uzhhorod 88000, Ukraine
[b] Institute of Chemistry, Slovak Academy of Sciences, Dúbravská cesta 9, Bratislava 84538, Slovakia
[c] Department of Inorganic Chemistry, Educational and Scientific Institute of Chemistry and Ecology, Uzhhorod National University, Pidhirna 46, Uzhhorod 88000, Ukraine
[d] Department of Biology and Chemistry, Ferenc Rákóczi II Transcarpathian Hungarian College of Higher Education, Kossuth Sq. 6, Beregove 90200, Ukraine
[e] Research Institute for Physics and Chemistry of Solid State, Uzhhorod National University, Pidhirna 46, Uzhhorod 88000, Ukraine
[f] Department of Ecology, Faculty of Humanity and Natural Sciences, University of Presov, 17th November str. 1, Presov 08116, Slovakia

ARTICLE INFO

Article history:
Received 31 August 2022
Revised 16 October 2022
Accepted 19 October 2022
Available online 25 October 2022

Keywords:
Cetylpyridinium
Charge transfer
Conductometry
Micelle
Perchlorate
XRD

ABSTRACT

Cetylpyridinium perchlorate has been synthesized and characterized by using the differential thermal analysis (DTA), X-ray powder diffraction (XRD) techniques, Fourier transform infrared spectroscopy (FT-IR), and ^{1}H and ^{13}C nuclear magnetic resonance (NMR) spectroscopy. The investigated salt melts congruently at 100 °C. The DTA and XRD results indicate that the cetylpyridinium perchlorate samples synthesized at different temperatures differ in crystallinity. It has been established that the crystallinity degree of the samples affects the decomposition temperature. The highest decomposition temperature (T_d = 265 °C) is observed for the sample crystallized at 20 °C. Cetylpyridinium perchlorate crystallizes in the monoclinic crystal system with the cell parameters a = 20.31 Å, b = 16.20 Å, c = 7.25 Å, β = 95.26°, Z = 4.

According to the DFT calculations, the interionic interactions in the structure are characterized by electron transfer from the perchlorate anion to the cetylpyridinium cation. This explains a noticeable difference in the ^{1}H NMR chemical shifts of the hydrogen atoms in the *ortho*-position (~0.2 ppm) and the α-methylene group (~0.1 ppm) of the DMSO solutions of the cetylpyridinium perchlorate and chloride salts micelles. The electronic structure analysis of cetylpyridinium perchlorate and cetylpyridinium chloride in terms of the "quantum theory of atoms-in-molecules" and the analysis of non-covalent interactions with the "reduced density gradient" method have revealed the presence of strong interactions between the ions in the DMSO solution.

1. Introduction

The cetylpyridinium (CP) cation has caught scientific interest for a long time due to the usage of its salts as components of cleaning and pharmaceutical formulations, which is defined by its surfactant [1–5] and antibacterial [6–10] properties. Moreover, cetylpyridinium salts of heteropolyacids are widely applied in organic syntheses as catalysts [11–13]. According to the Google Scholar database, over the period from 2018 to 2021, the number of the references containing the keywords "hexadecylpyridinium" or "cetylpyridinium" has increased from 2330 to 3200.

It should also be mentioned that due to the lipophilic nature of the CP cation, it is widely used in chemical analyses, primarily for association with anionic analytes and in ion-pair-based ionophores as a counter-ion. For example, in our previous work, we used CP chloride to titrate various lipophilic anions [14], and CP dipicrylamide was proposed as an ionophore in membrane CP-selective PVC electrode [15]. Furthermore, Chebotarev et al. [16] have used CP to modify silica in order to improve the analysis of food dyes, while Jayaprakash et al. [17] have successfully used a CP-modified carbon paste electrode as an ascorbic acid sensor. It is also worthy to note that the investigation of ionic associates of lipophilic cationic surfactants with lipophilic anions is an important task, because such ionic pairs are widely used as active compounds of electrochemical sensors [18–20] suitable, for example, to determine anionic surfactants with fast and robust potentiometric techniques [21].

The most common and commercially available forms of the CP cation are the monohydrate or anhydrous chloride and bromide salts, which are used as the primary source of the CP cation in various metathesis reactions. For example, Petersen et al. [22] have

* Corresponding author.
E-mail address: max.fizer@uzhnu.edu.ua (M. Fizer).

https://doi.org/10.1016/j.molliq.2022.120659
0167-7322/

proposed a CP salicylate ionic liquid additive to a paclitaxel-coated angioplasty balloon catheter. Yan et al. [8] explored the ionic liquid CP salicylate interactions with glycylglycine. Recently, we have synthesized and studied the CP picrate ionic liquid [23].

Taking all the above into consideration, in order to further expand the knowledge on the CP compounds, it was decided to explore the CP perchlorate salt (CPPC). CPPC has been mentioned in numerous studies [24–29]. For example, in 1968, Anacker and Ghose studied the influence of anions (including perchlorate) on the cetylpyridinium micelle size [24]. The works by Selig describe the usage of cetylpyridinium chloride (CPC) as a titrant for potentiometric determination of the perchlorate anion, which is obviously based on the formation of the CPPC precipitate [25,26]. Goga and co-workers have measured the dissociation constant of CPPC in methyl isobutyl ketone [27] and in a water-isopropanol mixture [28]. Furthermore, Mchedlov-Petrossyan et al. have explored the CPPC influence on negatively charged fullerene aggregates [29]. However, to the best of the authors' knowledge, the structural peculiarities and interionic interactions of the CPPC compound remain essentially unexplored. To fill the gap in the knowledge on the cation–anion interactions in CP-based salts, the CPPC ion pair was synthesized in the present study, and its structure was investigated by using the XRD, NMR, IR, and DFT methods.

2. Experimental

2.1. Reagents

All the reagents and solvents used in the present study were of a reagent-grade quality and have been purchased from Sphera Sim (Ukraine). Double distilled water was utilized in all preparations.

2.2. Instruments and measurements

The thermographic characterization of the CPPC samples has been performed by using the standard differential thermal analysis (DTA) technique [30] in the static air atmosphere with the heating rates of 4 °C/min and 12 °C/min. A combined chromel–alumel thermocouple (type K) was used as a temperature sensor, and pre-calcined Al_2O_3 was used as a reference material. Temperature values of thermal effects on the DTA heating and cooling curves were determined as proposed in [31]. The measurements were carried out in open quartz sample vessels. The thermal analysis was accompanied with the mass measurements before and after heating.

An "AXRD Benchtop" powder diffractometer equipped with a "MYTHEN2 R 1D" hybrid photon counting detector was used for recording the X-ray powder diffraction (XRD) patterns in the Bragg-Brentano geometry (θ/2θ) with the Ni-filtered CuKα radiation. The scanning was carried out in the 2θ angle range of 5–70 ° with the step size of 0.0199°. The PDAnalysis (Proto Manufacturing), EXPO2014 [32,33], and PowderCell 2.4 [34] software were utilized to analyze the experimental powder patterns.

The Fourier-transform infrared (FTIR) spectra were recorded on a "Shimadzu IRPrestige-21" spectrometer with a "Pike MIRacle" single reflection attenuated total reflectance accessory on zinc selenide crystal plate. A "Varian Mercury-400" instrument was used for recording the NMR spectra. Deuterated dimethyl sulfoxide (DMSO d_6) and tetramethylsilane were used as a solvent and standard, respectively. The solution of CPPC was prepared via dissolution of 38 mg of the salt in 0.6 mL of DMSO d_6.

An ADWA AD310 digital conductivity meter was used to measure the conductance of CPPC DMSO solutions at 25 °C. A thermostat cell with a temperature control preciseness of 0.1 °C was used to keep the DMSO solution at constant conditions.

2.3. Computational software and methods

The starting molecular geometries were created and pre-optimized using the Avogadro software [35]. DFT calculations have been done with ORCA 5.0.3 [36]. Hessians corresponding to optimized geometries were calculated analytically [37]. To speed up the calculations without accuracy reduction, the "resolution-of-id entity" and "chain-of-spheres approximations" methods have been turned on, and the SHARK module has been utilized throughout the calculations [38]. The "domain-based local pair natural orbital" (DLPNO) approximation was utilized during calculations with the second-order Møller-Plesset perturbation theory [39]. The investigation of the non-covalent interactions (NCI) with the reduced-density-gradient (RDG) method [40], related atoms-in-molecules (AIM) analysis [41], and charge decomposition analysis (CDA) [42] have been performed with the Multiwfn 3.8 program [43]. The Python code VibAnalysis has been used for the vibrational mode automatic relevance determination (VMARD) analysis of the DFT calculated IR spectrum and vibrations assignments [44]. The relevant input files were prepared using the Gabedit program [45], and visualization was done with the VMD software [46].

A DFT investigation has been performed to clarify the influence of the anion on the experimental NMR spectra. The M06-2X functional [47] combined with the 6-311G(d,p) basis set was used for the geometry optimization. This selection was dictated by the accuracy and diversity of usage of the M06-2X functional for various system types [48–52]. Moreover, the M06-2X functional is well known for its ability to reproduce weak non-covalent and ionic interactions [53,54]. Here it should be highlighted that the chosen method was robust enough for the systems under study; however, for larger systems (e.g., for those with a few long alkyl chains), the fast B97-3c method should be considered as a method of choice [55–57].

Both the explicit and implicit solvation models were employed to account for the solvent's influence. Two molecules of DMSO were coordinated near the site of cation–anion interaction, and a conductor-like polarizable continuum model (CPCM) was utilized to consider solvation implicitly [58,59].

The ^{1}H NMR chemical shifts have been calculated over the CPCM-M06-2X/6-311G(d,p) optimized geometries using the gauge-including atomic orbital (GIAO) approach [60,61] combined with various computational methods, namely Hartree-Fock, M06-2X, M06-L [47], DLPNO-MP2 [62], and the triple-zeta segmented contracted basis set pcSseg-2, which was optimized for nuclear magnetic shielding predictions [63]. The M06-2X/6-311G(d,p) NMR chemical shifts were also considered for comparison.

2.4. Synthesis of cetylpyridinium perchlorate (CPPC)

Two CPPC samples were synthesized from solutions at temperatures of 20 °C (CPPC20) and 80 °C (CPPC80). An excess of sodium perchlorate 1.0 M solution (2 mL, 2 mmol) was dropwise added to the stirred 0.01 M solution of CPC (100 mL, 1 mmol) at a chosen temperature. The resulting white precipitate was filtered and washed with a small quantity of cold double distilled water. The resulting white powder cake was air-dried. The yield of CPPC20 has been found to be of 90 % (0.364 g), whereas the yield of CPPC80 has resulted in 78 % (0.315 g). Mp 100 °C. ^{1}H NMR (DMSO d_6, 400 MHz), δ (ppm): 9.08 (2H, d, *o*-$CH_{pyridinium}$), 8.60 (1H, t, *p*-$CH_{pyridinium}$), 8.16 (1H, t, *m*-$CH_{pyridinium}$), 4.59 (2H, t, CH_2N), 1.91 (2H, m, *β*-CH_2), 1.24–1.27 (26H, m, 13[CH_2]), 0.86 (3H, t, CH_3). ^{13}C NMR (DMSO, 100 MHz), δ (ppm): 145.42, 144.66, 128.04, 60.77, 31.25, 30.64, 29.00, 28.96, 28.87, 28.74, 28.66, 28.34, 25.36, 22.04,

13.87. Elemental analysis, found (%): C, 62.30; H, 9.63; N, 3.28; molecular formula $C_{21}H_{38}ClNO_4$ requires (%): C, 62.43; H, 9.48; N, 3.47.

3. Results and discussion

3.1. Synthesis of the cetylpyridinium perchlorate ionic liquid

To check the possible influence of reaction conditions on the final product, the synthesis of the CPPC ionic pair by a salt metathesis reaction between cetylpyridinium chloride and sodium perchlorate was taken at two different temperatures. Consequently, two samples were obtained, and these were the current study's object. The structural formula of the CPPC ionic pair is presented in Fig. 1.

3.2. Differential thermal analysis

The DTA investigations were carried out to determine the phase transitions temperatures of the two prepared CPPC samples. Defined quantities of CPPC were heated to 310 °C with the heating rate of 12 °C/min. Both of the DTA heating curves contain two thermal effects (Fig. 2). It must be clarified that the CPPC DTA heating curves do not contain any characteristic thermal effects of the initial compounds, namely cetylpyridinium chloride monohydrate [23] and $NaClO_4$ [64].

The temperatures of the endothermic effects do not differ significantly: 100 °C for the CPPC20 sample and 99 °C for the CPPC80 sample. This temperature difference can be caused by the DTA device sensitivity. However, the temperatures of the exothermic effects observed for the above CPPC samples (265 °C and 239 °C, respectively) have been found to differ significantly: ΔT = 26 °C (Fig. 2). The changes in the external look of the samples after heating (from white to black) and the weight loss of Δm = 82.1 % indicate that CPPC undergoes an irreversible decomposition at the temperature of the exothermic effect. In turn, the sharpness of the exothermic effects indicates a rapid decomposition of the investigated samples. The difference in the decomposition temperatures will be discussed below.

To prevent the decomposition of CPPC, as well as to determine the nature of the endothermic effect, the second series of heating of the CPPC samples was carried out only to 150 °C (see the insets of Fig. 2). The heating rate was chosen at 4 °C/min to avoid decomposition of the samples. The DTA heating curve of CPPC crystalized at 20 °C contains one endothermic effect (101 °C) which has a corresponding exothermic effect at 78 °C (the inset of Fig. 2a). After the thermal treatment, the resulting sample was melted and had white with a yellowish tinge color. Since this effect is reversible and does not cause any sample weight and color changes, the endothermic effect corresponds to the melting of CPPC. The sharpness of the exothermic peak shows a fairly high crystallization rate of CPPC. The investigated CPPC sample exhibits a significant undercooling ΔT = 23 °C, which is often inherent for pure materials [65]. An analogous DTA experiment was carried out for the CPPC sample obtained at a higher temperature (the inset of Fig. 2b). As seen, the results obtained for both of the investigated samples are similar, thus confirming the congruent melting of CPPC at 100 °C.

By comparing the areas of the DTA peaks recorded for CPPC and for the standard material under the same conditions, the heat of fusion of CPPC has been estimated. As a standard material [30], a known amount of pure indium (T_m = 156.6 °C, Δh_m = 28.66 J/g [66]) was used. The heat of fusion values were found to be 170.8 J/g and 115.4 J/g for the CPPC20 and CPPC80 samples, respectively. Because of the above significant difference between the heat of fusion values, the CPPC80 sample was repeatedly scanned by DTA; and the heat of fusion value determined for this recrystallized CPPC sample equals 170.9 J/g, in excellent agreement with the value obtained for the CPPC sample synthesized at 20 °C.

As the heating rate was constant in both cases, the observed difference in the CPPC decomposition temperatures can be conditioned by different sizes of crystallites and/or by different amounts of the amorphous phase content of the samples synthesized at different temperatures. This suggestion was confirmed by the XRD analysis (see below).

3.3. X-ray diffraction measurements

The powder XRD measurements were used for phase identification and for determination of the cell parameters of the synthesized CPPC samples. The XRD patterns obtained for both of the CPPC samples are shown in Fig. 3. The phase analysis was carried out by comparing the observed XRD patterns of CPPC with the patterns of the starting compounds, CPC monohydrate [67] and $NaClO_4$ [68]. It has been revealed that the XRD patterns of both CPPC samples do not contain peaks of the initial phases.

The XRD patterns of both CPPC samples reveal sharp diffraction peaks indicating the presence of a well-crystallized CPPC fraction. However, the wavy background curves (see Fig. 3) clearly indicate the presence of certain amounts of the amorphous CPPC component in the samples. The crystallinity degrees calculated by using the PDAnalysis software for the CPPC samples obtained at 20 °C and 80 °C are ~ 65 % and ~ 59 %, respectively. Both of the XRD patterns are characterized by the same system of reflexes. Analysis of these patterns has revealed the fact that the diffraction peaks are better resolved and manifested for the CPPC20 sample (Fig. 3), in agreement with the above conclusion about the crystallinity degrees.

Both the one-time-melted CPPC samples were additionally investigated by XRD analysis. The powder diffraction patterns of the CPPC samples crystallized from the melt are similar to each other and to the pattern of the CPPC80 sample. For both melted samples, the calculated crystallinity is ~ 68 %, and the peak inten-

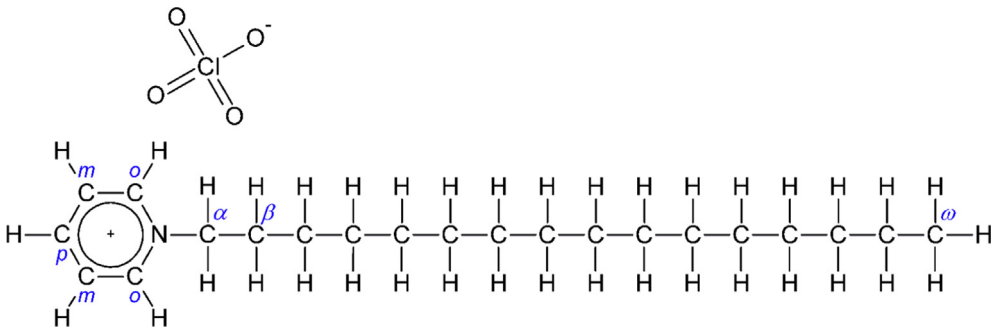

Fig. 1. Structure and numbering of the CPPC ionic pair.

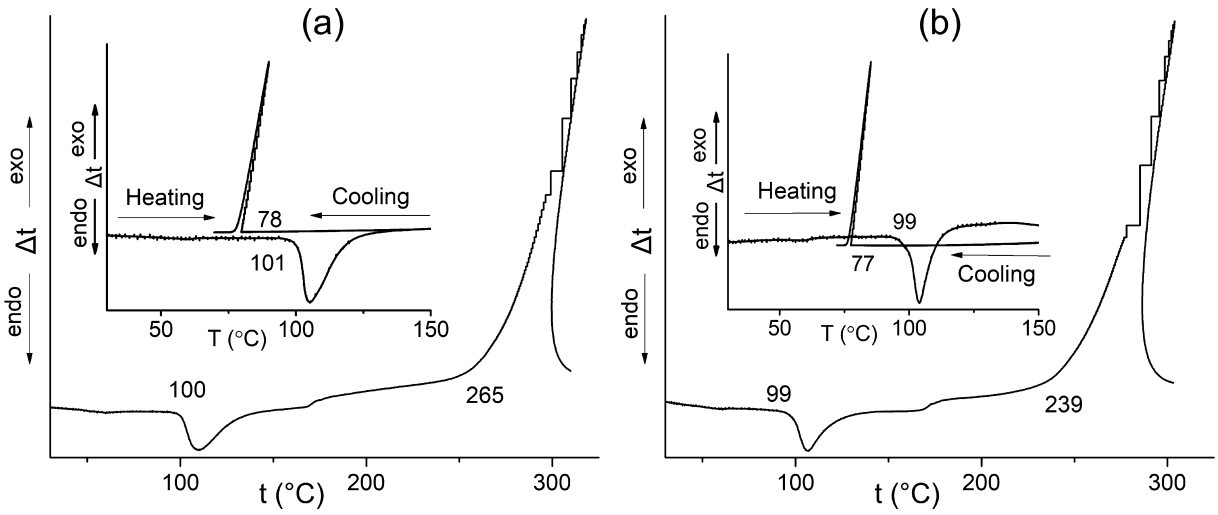

Fig. 2. DTA curves of the CPPC samples obtained at 20 °C (a) and 80 °C (b); insets – the curves obtained for the corresponding CPPC samples in the temperature range of 30–150 °C.

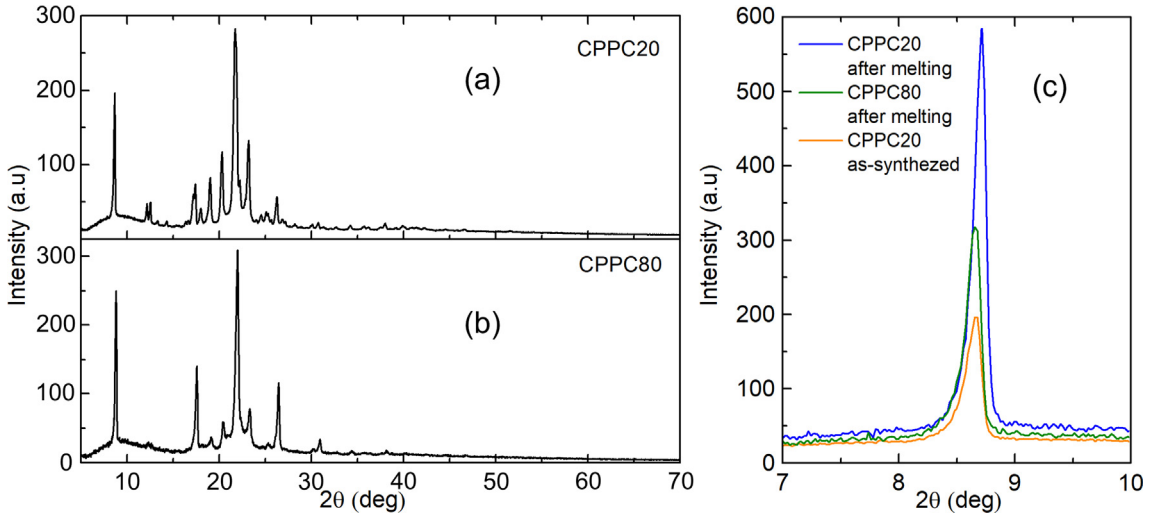

Fig. 3. XRD powder patterns of the CPPC samples synthesized at 20 °C (a) and 80 °C (b), and the overlapped peaks (c).

sities are higher than those observed for the as-synthesized CPPC sample (Fig. 3c). An increase of crystallinity after melting for the CPPC20 and CPPC80 samples is confirmed by a decrease of the FWHM (full width at half maximum) values which are 0.1397° and 0.1635° before melting and 0.1172° and 0.1348° after melting, respectively. The fact that only a few peaks appear more intense after melting is caused by the samples' preferred orientation due to plate-shaped crystallites.

The cell parameters of the CPPC20 sample were determined from the XRD pattern by using the autoindexing procedure of the EXPO2014 program. The indexing has shown that CPPC crystallizes in the monoclinic crystal system (syngony) with the cell parameters a = 20.31 Å, b = 16.20 Å, c = 7.25 Å, β = 95.26°, and with the cell volume V = 2375 Å^3. Calculated from the density measurements (d = 1.1445 g/cm^3) and cell volume, the number of formula units in the unit cell is Z = 4.

3.4. Fourier-transform infrared spectroscopy

To assign the IR peaks to specific vibrations, the vibrational mode automatic relevance determination (VMARD) analysis of the DFT calculated frequencies has been performed with the VibAnalysis program. The model CPPC structure was arranged to maximize the electrostatic interionic attraction; thus, the perchlorate anion was located as close as possible to the *ortho*-position of the pyridinium ring and the α-methylene group. The DFT geometry and frequencies were calculated with the B3LYP functional [69] and the 6-311G(d,p) basis set on H, C, and N atoms, whereas the diffuse functions have been added to O and Cl atoms. The dielectric constant was set to infinity to model the crystalline state of the CPPC via the conductor-like polarizable continuum model (CPCM) [58,59]. The selection of this level of theory was dictated by its good performance in predicting vibrational frequencies [70–73]. The optimized geometry and the assignment of vibrational frequencies are presented in the supplementary materials (see Tables S1 and S2).

The FT-IR ATR spectra of both CPPC20 and CPPC80 samples were identical so we will discuss only the CPPC20 spectrum in detail. Fig. 4 presents the overlapped FT-IR ATR spectra of the solid-state CPPC sample (Fig. 4a) and CP chloride monohydrate (CPCH) (Fig. 4b). The characters of both these spectra are similar, with only a marginal difference in some peaks' wavenumbers,

which testifies the similarity of the CPPC and CPCH structures. Here we will focus on the CPPC peaks. Thus, very weak peaks at 2953, 3075, and 3137 cm^{-1} correspond to the C—H stretching vibrations of the pyridinium ring. The symmetric and asymmetric H—C—H stretching vibrations of the cation's alkyl chain can be observed as medium bands at 2851 and 2916 cm^{-1}, respectively. A weak peak at 1640 cm^{-1} corresponds to the C=C and C=N stretching vibrations in the aromatic ring. The bends in the region of 1223–1507 cm^{-1} correspond to the C—C—H vibrations of the ring and to the H—C—H vibrations (bending, wagging, twisting) of the alkyl chain. The peak at 1182 cm^{-1} can be addressed to the $H_2C—N^+$ stretching vibrations. The strong peak at 1087 cm^{-1} is related to the asymmetric stretching in the ClO_4^- anion. The weak band at 823 cm^{-1} should be addressed to the $H—CH_2—C$ bending of the terminal methyl group. The strong peaks at 784 cm^{-1} and 691 cm^{-1} correspond to the ring's out-of-plane C—H bendings. Rocking H—C—H vibrations in the alkyl chain cause the medium band at 720 cm^{-1}.

3.5. Nuclear magnetic resonance study

CPPC was synthesized via the substitution of the chloride anion in CPCH with the perchlorate anion; this substitution is expected not to make a difference between the NMR spectra of the two compounds. For a more convenient comparison, the ^1H NMR spectra of $(CD_3)_2SO$ solutions of CPPC and CPCH were overlapped in Fig. 5. The ^1H NMR spectrum of CPCH was taken from our previous work [23]. The peaks at 2.50 ppm and 3.29/3.39 ppm correspond to the solvent and residual water signals, respectively. As expected, the signals of the aromatic pyridinium ring are located in the downfield area of the spectrum. In contrast, the signals of the alkyl chain are located in the upfield area. Thus, the triplet at 0.86 ppm with a relative intensity of 3 corresponds to the terminal methyl group of the cetyl chain. The intense peak at 1.24–1.27 ppm is the overlapped signals of the C3-C15 methylene groups of the cetyl chain. The multiplet at 1.91 ppm with a relative intensity of 2 corresponds to the signal of the cetyl chain's β-methylene (*C*2) bridge. The signal of the α-methylene group (C1) of the chain is downshifted due to the electron-withdrawing character of the pyridinium ring and appears at 4.59 ppm as a triplet with a relative intensity of 2. *ortho*-, *meta*-, and *para*-protons of the pyridinium ring appears in the spectrum at 9.07 ppm (doublet), 8.16 ppm (triplet), and 8.63 ppm (triplet), respectively. Here we have to highlight noticeable upfield shifts of the α-methylene group (about 0.1 ppm) and *ortho*-protons (about 0.2 ppm) of the ring compared to the corresponding signals in the CPCH spectrum.

Fig. 6 represents the overlapped ^{13}C NMR spectra of the CPPC and CPCH solutions in $(CD_3)_2SO$. Again, the aromatic pyridinium ring signals are located in the downfield area: the peaks at 128.04, 144.06, and 145.42 ppm correspond to the *meta*-, *ortho*-, and *para*-carbon atoms of the pyridinium rings. The peak at 60.77 ppm corresponds to the α-CH_2 group signal. The peaks in the region of 22.04–31.25 ppm are related to the chain's signals of *C*2-C15 carbon atoms. The most upfield peak at 13.87 ppm corresponds to the terminal methyl group carbon atom. Small but noticeable differences in the spectra of CPPC and CPCH should be highlighted. Compared with the spectrum of CPCH, the most significant downfield shift for 0.29 ppm is observed for the α-methylene group signal. Oppositely, the upfield differences of 0.17 and 0.16 ppm should be addressed to the ring's *ortho*-carbons and the *β*-methylene group carbon atom, respectively.

As was suggested earlier, the observed differences in the NMR chemical shifts between the different salts of cetylpyridinium can be caused by the aggregation of surfactant cetylpyridinium salts into micelles [23]. In order to check whether CPPC and CPCH are aggregated in the DMSO solutions, conductometric measurements were performed (see below).

3.6. Conductivity measurements

It was suggested that the observed differences in the NMR chemical shifts might be caused by the association and micelle formation of the CPPC molecules in the DMSO solution. To verify this hypothesis, the electrical conductivity (κ) of the CPPC solutions in DMSO was measured, as well as the corresponding molar conductivity (Λ_m) values were calculated from the relationship $\Lambda_m = \kappa/C$. However, the trivial dependencies like $\kappa = f(C_{CPPC})$ (Fig. 7a), $p\kappa = f(pC_{CPPC})$ (see Fig. S1a in supplementary materials), or $\Lambda_m = f(\sqrt{C})$ (see Fig. S1b in supplementary materials) were not very useful in the direct determination of the critical micelle concentration (CMC) value. On the other hand, it was shown that the plots of the first and second derivatives of the conductivity over the concentration are extremely useful in determining the cationic surfactants' CMC values [74]. Thus, the first and second derivatives of conductance over the concentration of the CPPC solution are shown in Fig. 7b. The infection points of the $d\kappa/dC$ curve give the CMC region determined from the first derivation, whereas the extremum point of the $d^2\kappa/dC^2$ curve corresponds to the CMC value (0.014 mol/L). In our previous investigation [23], the first CMC of the DMSO solution of CPC was estimated to be equal to 0.01 mol/L. As mentioned in the experimental section, the DMSO solution of CPPC was prepared by mixing 38 mg of CPPC and

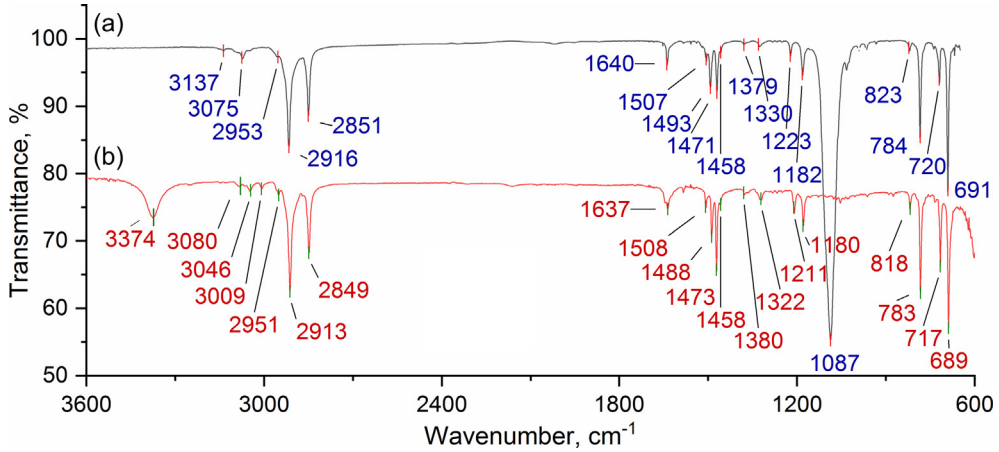

Fig. 4. FT-IR spectra of CPPC (a) and CPCH (b).

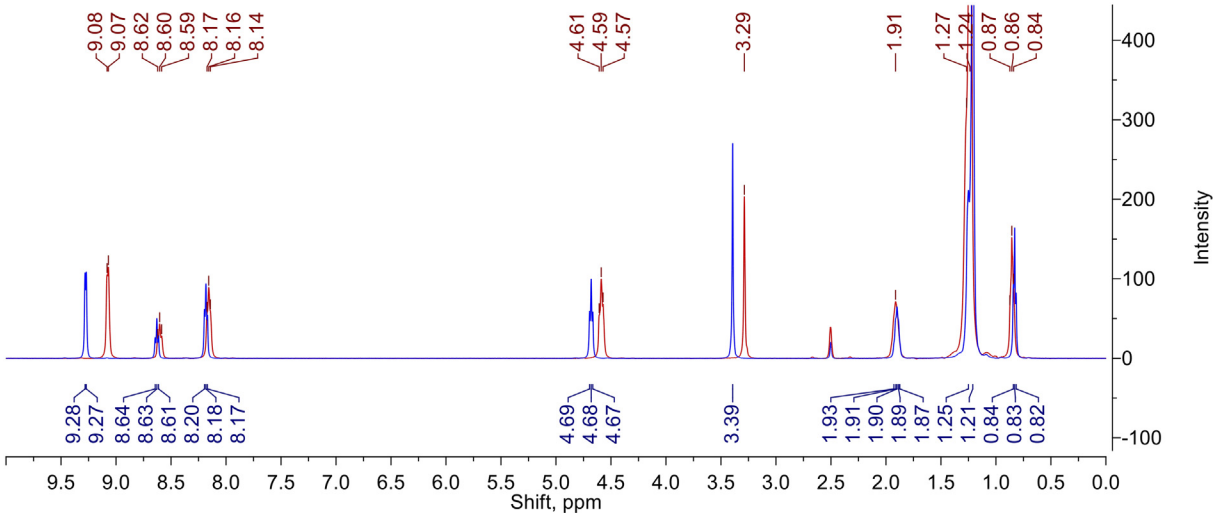

Fig. 5. Overlapped ^{1}H NMR spectra of CPPC (red) and CPCH (blue). (For interpretation of the references to color in this figure legend, the reader is referred to the web version of this article.)

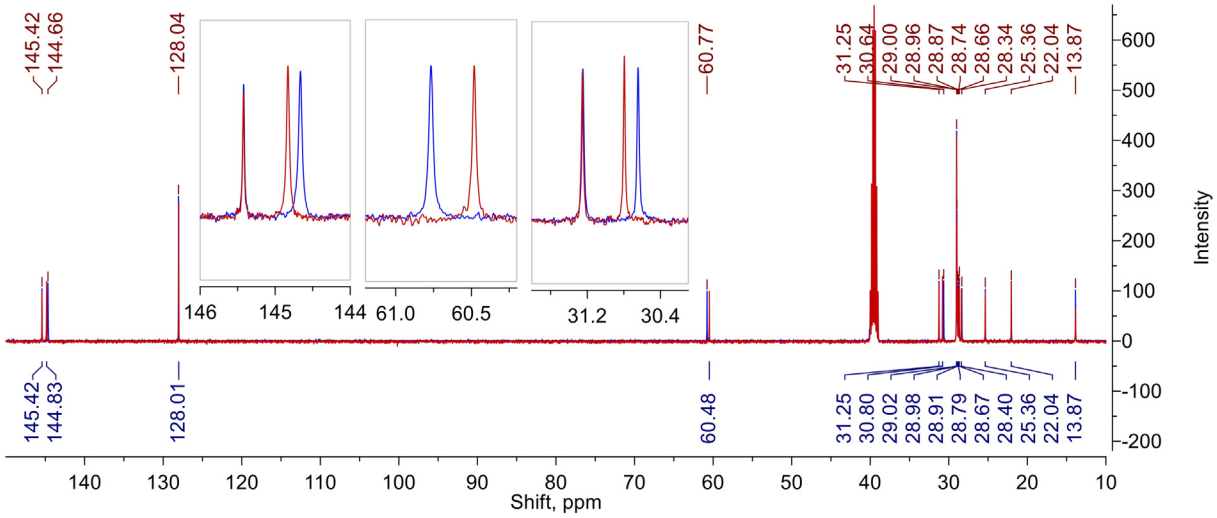

Fig. 6. Overlapped ^{13}C NMR spectra of CPPC (red) and CPCH (blue). (For interpretation of the references to color in this figure legend, the reader is referred to the web version of this article.)

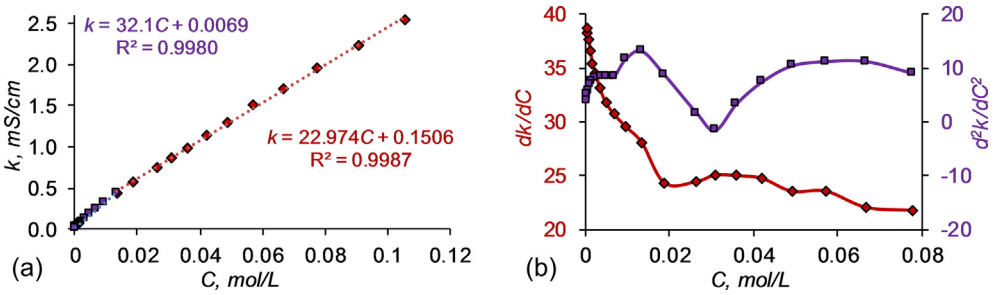

Fig. 7. Conductivity measurements: (a) the relationship between the conductivity κ and concentration C. The equations that represent the linear parts of the conductivity curve below and above the CMC value are shown in purple and red, respectively; (b) first (red) and second (purple) derivatives of the conductance over the concentration. (For interpretation of the references to color in this figure legend, the reader is referred to the web version of this article.)

0.6 mL of DMSO d_6, corresponding to the CPPC concentration of 0.157 mol/L.

Similarly, the concentration of the reference CPC solution equals 0.154 mol/L. Both these values are quite close and much higher than the determined CMC values, which means that the recorded NMR spectra correspond to micelles of CPC and CPPC. This allows us to conclude that the observable differences in the chemical shifts are caused by the anion's influence in the electrical double layer of a micelle. To validate this assumption, the DFT computations have been performed.

Analysis of the conductivity curve $\kappa = f(C)$ in the regions below and above CMC allows for determining the degree of counter-ion binding (β). According to the equation $\beta = 1 - S_2/S_1$, S_1 is the slope of the conductivity curve below the CMC, and S_2 is the conductivity curve above the CMC. According to the slopes' values presented in Fig. 7a, the degree of counter-ion binding was calculated to equal 0.284.

3.7. DFT NMR modeling

Atomistic models representing the interaction between the CP cation and the anion (Cl^- or ClO_4^-) in a micelle were organized to provide a maximal electrostatic interaction between the cation and anion. According to our previous study, the areas with the maximal electrostatic potential values are located near the hydrogen atoms in the *ortho*-position of the pyridinium ring and the α-methylene group of the cetyl chain [75]. For this reason, to maximize the electrostatic interionic attraction, the anion (Cl^- or ClO_4^-) was located as close as possible to the *ortho*-position of the pyridinium ring and the α-methylene group. The geometries of the models were optimized, and respective second derivatives were calculated analytically to verify that the obtained structures are true minima and that there are no imaginary frequencies in the corresponding Hessians. The atoms' Cartesian coordinates of the optimized systems are presented in the supplementary materials (Tables S3 and S4).

Table 1 summarizes the chemical shifts and corresponding differences computed with the aforementioned methods. The signal of the cetyl chain's terminal methyl group was considered as an internal standard. All the considered methods correctly predict the experimentally observed upfield shift during the substitution of the chloride anion with the perchlorate anion. It must be noted, however, that the theoretical techniques considerably overestimate the values of the chemical shifts difference; nevertheless, all the methods, at least qualitatively, predict the higher upfield shift of the *ortho*-position hydrogen atom as compared with the α-methylene group hydrogen. Taking into account that the chemical shifts' differences were most correctly predicted by the M06-2X/6-311G(d,p) level of theory, the electron densities generated at this level were used for further analysis of the model systems.

Optimized geometries of the model CPC and CPPC ion pairs with two DMSO molecules are presented in Fig. 8. To analyze the interactions between the CP cation and the anion (Cl^- or ClO_4^-), the topology analysis in terms of the "Atoms-in-Molecules" theory (AIM) [41,76], as well as non-covalent interaction via the reduced density gradient method (NCI-RDG) have been performed [40,77]. The results of the AIM analysis of the considered ion pairs are presented in Fig. 8a and Fig. 8b: bond critical points (BCPs) are shown as blue dots, ring critical points as red dots, and cage critical points as pink dots. In the present study, we were focused on the analysis of the BCPs between the CP cation and the anions considered. Thus, in the case of CPC, four interionic BCPs have been observed (Fig. 8a, points p1–p4), whereas, in the CPPC ion pair, seven interionic BCPs have been found (Fig. 8a, points p5–p11). The characteristics of the BCPs are summarized in Table 2. In general, it should be noticed that the BCPs are located between the anion (atom Cl31) and hydrogen atoms in the *ortho*-position of the pyridinium ring, α-, β-, and γ-methylene groups. Considering only the electron density values at BCPs, it is hard to precisely quantify the strength of interionic interactions in CPC and CPPC. For example, the maximal value of electron density (0.01278 a.u.) was observed in the case of CPC between the chloride anion and H8 hydrogen atom in the *ortho*-position of the pyridinium ring. However, in the case of CPPC, two oxygen atoms of the anion, O65 and O62, interact with the H8 atom, and corresponding BCPs are characterized by the electron density values of 0.01026 and 0.00620 a.u., respectively. The atoms were numbered according to Cartesian coordinates presented in Tables S3 and S4 (supplementary materials).

The above-discussed AIM and NCI-RDG analyses show the presence of strong interionic interactions in the CPC and CPPC models/micelles. However, to clarify the observable upfield shifts in the NMR spectra, the charge decomposition analysis (CDA) was performed using the Multiwfn software [43]. At this stage, we were mainly interested in studying interactions between the CP cation and the considered anions. The electron density generated at the CPCM-M06-2X/6-311G(d,p) level of theory was used. The data obtained from the CDA are summarized in Table 3. As expected, in both CPC and CPPC, the amount of donated electrons from the cation to the anion is characterized by small negative values, which shows that the donation of electrons from a cation to an anion is an unfavorable process. Oppositely, donating electrons from an anion to the cetylpyridinium cation is much more favorable, especially in the case of the perchlorate anion.

To summarize, the difference between the considered donations shows that net transferred electrons from the anion to the cation are equal to about 0.0526 and 0.0227 in the cases of CPPC and CPC, respectively. The negative values of the overlap population between the occupied fragment orbitals of the two ions in the corresponding complex orbital reveal that the repulsive effect dominates the overall interaction between the occupied orbitals of the ions, resulting in the moving of the corresponding electrons from the overlapping region towards the non-overlapping ones. The higher electron donation in the case of perchlorate explains the observed upfield NMR shift compared with chloride. Thus, the higher electron donation to the interacting hydrogen atoms in

Table 1
^{1}H NMR chemical shifts of the hydrogen atoms in *ortho*-position of the pyridinium ring and the α-methylene group in the CPC and CPPC model systems with two DMSO molecules, calculated with the M06-L, M06-2X, Hartree-Fock, and DLPNO-MP2 methods. The CPCM solvation is included in all the calculations. All values are given in ppm.

	M06-L/pcSseg-2	M06-2X/pcSseg-2	Hartree-Fock/pcSseg-2	DLPNO-MP2/pcSseg-2	M06-2X/6-311G(d,p)	Experimental
CPC *ortho*-position	10.44	11.31	10.74	10.52	11.07	9.28
CPPC *ortho*-position	9.65	10.69	10.16	9.85	10.77	9.08
difference *ortho*-position	0.80	0.62	0.58	0.68	0.31	0.20
CPC α-CH_2 group	5.24	5.45	5.11	5.54	5.26	4.68
CPPC α-CH_2 group	4.88	5.02	4.67	5.12	4.98	4.59
difference α-CH_2 group	0.35	0.43	0.44	0.43	0.29	0.09

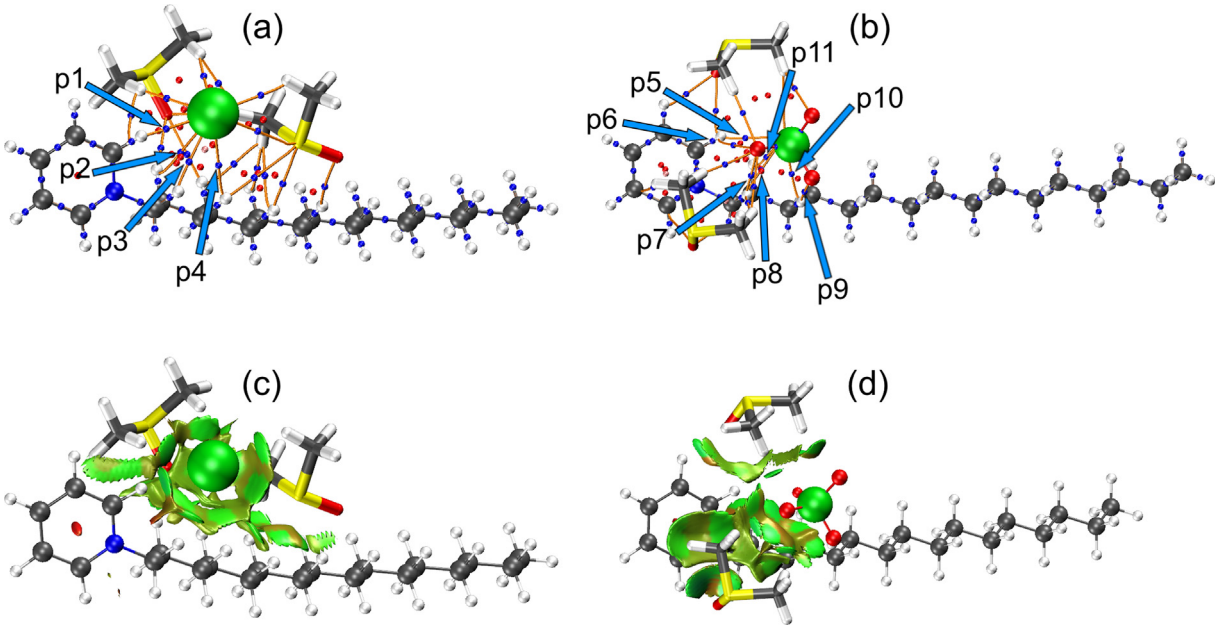

Fig. 8. AIM analysis of CPC with two DMSO molecules (a); AIM analysis of CPPC with two DMSO molecules (b); NCI-RDG analysis of CPC with two DMSO molecules (c); NCI-RDG analysis of CPPC with two DMSO molecules (d); CPC and CPPC are shown in the "balls-and-sticks" style, whereas the DMSO molecules are shown in the "tubes" style.

Table 2
Characteristics of the interionic BCPs determined for the CPC and CPPC ion pairs, including two molecules of DMSO. The interacting atoms corresponding to the BCPs are shown.

CPC			CPPC					
BCP	Interacting atoms	electron density, a.u. × 100	BCP	Interacting atoms	electron density, a.u. × 100	BCP	Interacting atoms	electron density, a.u. × 100
p1	Cl31–H8	1.278	p5	O65–H8	1.026	p9	O63–H21	0.839
p2	Cl31–H14	0.892	p6	O62–H8	0.620	p10	O65–H21	0.781
p3	Cl31–H17	0.496	p7	O62–H14	0.958	p11	O65–H17	1.058
p4	Cl31–H21	0.453	p8	O65–H14	0.885			

Table 3
Charge decomposition analysis for the CPPC and CPC models with two DMSO molecules: cation-to-anion donation, anion-to-cation donation, the difference between the donations, and the overlap population. All the values are given in electrons.

	Cation-to-anion donation	Anion-to-cation donation	Difference	Overlap population
CPPC	−0.002139	0.050415	−0.052555	−0.081124
CPC	−0.004204	0.018464	−0.022668	−0.100681

the *ortho*-position of the pyridinium ring and the α-methylene group causes the shielding of the protons and results in their upfield chemical shifts.

4. Conclusions

According to the literature data, the cetylpyridinium perchlorate salt is an interesting compound with broad scientific exploration areas. However, there was a gap in the fundamental properties of this ionic pair, which was tried to get filled in the present study. Two samples of cetylpyridinium perchlorate salt were synthesized at 20 °C and 80 °C, characterized by different crystallinity degrees. According to the thermal investigations, CPPC melts congruently at 100 °C. It has been established that the synthesis of CPPC at a lower temperature leads to a higher crystallinity degree of the sample. The sample with a higher crystallinity degree (i.e., that formed at 20 °C) is characterized by a higher decomposition temperature (T_d = 265 °C) as compared to the sample obtained at 80 °C (T_d = 239 °C). Cetylpyridinium perchlorate crystallizes in the monoclinic crystal system. The FT-IR and NMR analyses unequivocally confirm the presence of the unmodified, non-covalently bonded cetylpyridinium and perchlorate ions.

The experimentally observed difference in ^{1}H NMR chemical shifts of the hydrogen atoms in the *ortho*-position of the pyridinium ring and the α-methylene group of CPPC compared to CPC, has been explained by a high interionic electron transferring from the anion to cation, which is theoretically calculated for the associated forms of CPPC and CPC. The existence of CPPC and CPC in partly associated micellized structures has been confirmed by the conductivity measurements, which allowed to estimate of a critical micelle concentration of CPPC in DMSO as 0.157 mol/L, and the degree of counter-ion binding was found to be equal to 0.284. Considering that the determined critical micelle concentration of CPPC and CPC is lower than the concentrations of the solutions studied by NMR, we can assume that the experimentally observed peak differences in the NMR spectra are primarily due to the donating (shielding) activity of the anions rather than the micelle formation itself.

Comparing the ^{1}H NMR chemical shifts calculated at the CPCM-M06-L/pcSseg-2, CPCM-M06-2X/pcSseg-2, CPCM-Hartree-Fock/pcSseg-2, CPCM-DLPNO-MP2/pcSseg-2, and CPCM-M06-2X/6-311G(d,p) levels of theory with the experimental values, one must conclude that the results obtained with the CPCM-M06-2X/6-311G (d,p) method are the most accurate.

CRediT authorship contribution statement

Oksana Fizer: Investigation, Writing – original draft, Writing – review & editing. **Maksym Fizer:** Conceptualization, Supervision, Writing – original draft. **Michael Filep:** Investigation, Writing – original draft. **Vasyl Sidey:** Investigation, Writing – original draft, Writing – review & editing. **Ruslan Mariychuk:** Investigation, Writing – original draft.

Data availability

No data was used for the research described in the article.

Declaration of Competing Interest

The authors declare that they have no known competing financial interests or personal relationships that could have appeared to influence the work reported in this paper.

Acknowledgments

This study was partially supported by the Ministry of Education and Science of Ukraine [Projects GR-0120U100431], the Slovak Academic Information Agency (National Scholarship Programme of the Slovak Republic, Grants ID 32706 and ID 35558], and the Scientific Grant Agency of the Ministry of Education, Science, Research and Sport of the Slovak Republic and Slovak Academy of Sciences (projects VEGA 02/0137/20 and VEGA 1/0116/22).

Appendix A. Supplementary material

Supplementary data to this article can be found online at https://doi.org/10.1016/j.molliq.2022.120659.

References

[1] W. Zhang, S. Zhang, J. Wang, J. Dong, B. Cheng, L. Xu, A. Shan, A novel adsorbent albite modified with cetylpyridinium chloride for efficient removal of zearalenone, Toxins 11 (2019) 674, https://doi.org/10.3390/toxins11110674.
[2] S. Chowdhury, G. Halder, T. Mandal, J. Sikder, Cetylpyridinium bromide assisted micellar-enhanced ultrafiltration for treating enrofloxacin-laden water, Sci. Total. Environ. 687 (2019) 10–23, https://doi.org/10.1016/j.scitotenv.2019.06.074.
[3] A.J. Kora, K. Madhavi, N.N. Meeravali, S.J. Kumar, In situ synthesis and preconcentration of cetylpyridinium complexed hexaiodo platinum nanoparticles from spent automobile catalytic converter leachate using cloud point extraction, Arabian J. Chem. 13 (2020) 4594–4605, https://doi.org/10.1016/j.arabjc.2019.10.008.
[4] A. Rehman, M. Usman, T.H. Bokhari, H.M.A. Rahman, A. Mansha, M. Siddiq, A. Rasheed, M.U. Nisa, Effects of nonionic surfactant (TX-100) on solubilizing power of cationic surfactants (CTAB and CPC) for Direct Red 13, Colloid. Surface A 586 (2020), https://doi.org/10.1016/j.colsurfa.2019.124241.
[5] T.M. de Miranda, A.R. de Oliveira, J.R. Pereira, J.G. da Silva, I.S. Lula, C.S. Nascimento Jr., A.M.L. Denadai, Inclusion vs. micellization in the cethylpyridine chloride/β-cyclodextrin system: a structural and thermodynamic approach, J. Mol. Struct. 1184 (2019) 289–297, https://doi.org/10.1016/j.molstruc.2019.02.033.
[6] K. Matsuo, K. Yoshihara, N. Nagaoka, Y. Makita, H. Obika, T. Okihara, A. Matsukawa, Y. Yoshida, B. Van Meerbeek, Rechargeable anti-microbial adhesive formulation containing cetylpyridinium chloride montmorillonite, Acta Biomater. 100 (2019) 388–397, https://doi.org/10.1016/j.actbio.2019.09.045.
[7] G.P.J. Langa, J. Cavagni, F.W.M.G. Muniz, H.J.R. Oballe, S. Anagnostopoulos Friedrich, A.C. Nicolini, D.P. Thomé, L.L. Sossai, A.G. Rup, Z. Malheiros, B. Stewart, L. Kilpatrick, M. Ryan, C.K. Rösing, Antiplaque and antigingivitis efficacy of cetylpyridinium chloride with zinc lactate compared with essential oil mouthrinses: Randomized clinical trial, J. Am. Dent. Assoc. 152 (2021) 105–114, https://doi.org/10.1016/j.adaj.2020.09.021.
[8] Z. Yan, X. Cao, M. Sun, L. Zhang, Physicochemical study on molecular interactions in ternary aqueous solutions of the pharmaceutically active ionic liquid cetylpyridinium salicylate and amino acid/glycylglycine at different temperatures, J. Mol. Liq. 326 (2021), https://doi.org/10.1016/j.molliq.2020.115258.
[9] B. Teoman, Z.P. Muneeswaran, G. Verma, D. Chen, T.V. Brinzari, A. Almeda-Ahmadi, J. Norambuena, S. Xu, S. Ma, J.M. Boyd, P.M. Armenante, A. Potanin, L. Pan, T. Asefa, V. Dubovoy, Cetylpyridinium trichlorostannate: synthesis, antimicrobial properties, and controlled-release properties via electrical resistance tomography, ACS Omega 6 (2021) 35433–35441, https://doi.org/10.1021/acsomega.1c04034.
[10] V. Dubovoy, S. Nawrocki, G. Verma, L. Wojtas, P. Desai, H. Al-Tameemi, T.V. Brinzari, M. Stranick, D. Chen, S. Xu, S. Ma, J.M. Boyd, T. Asefa, L. Pan, Synthesis, characterization, and investigation of the antimicrobial activity of cetylpyridinium tetrachlorozincate, ACS Omega 5 (2020) 10359–10365, https://doi.org/10.1021/acsomega.0c00131.
[11] O. Paley, Cetylpyridinium chloride, Synlett 25 (2014) 599–600, https://doi.org/10.1055/s-0033-1340488.
[12] B. Guérin, D.M. Fernandes, J.-C. Daran, D. Agustin, R. Poli, Investigation of induction times, activity, selectivity, interface and mass transport in solvent-free epoxidation by H_2O_2 and TBHP: a study with organic salts of the $[PMo_{12}O_{40}]^{3-}$ anion, New J. Chem. 37 (2013) 3466–3475, https://doi.org/10.1039/C3NJ00523B.
[13] Z.P. Pai, D.Y. Yushchenko, T.B. Khlebnikova, V.N. Parmon, N-phosphonomethyl iminodiacetic acid N-oxide synthesis in the presence of bifunctional catalysts based on tungsten complexes, Catal. Commun. 71 (2015) 102–105, https://doi.org/10.1016/j.catcom.2015.08.021.
[14] O. Fizer, F. Fizer, V. Sidey, Y. Studenyak, Predicting the end point potential break values: a case of potentiometric titration of lipophilic anions with cetylpyridinium chloride, Microchem. J. 160 (2021), https://doi.org/10.1016/j.microc.2020.105758.
[15] M. Fizer, O. Fizer, V. Sidey, R. Mariychuk, Y. Studenyak, Experimental and theoretical study on cetylpyridinium dipicrylamide – A promising ion-exchanger for cetylpyridinium selective electrodes, J. Mol. Struct. 1187 (2019) 77–85, https://doi.org/10.1016/j.molstruc.2019.03.067.
[16] A. Chebotarev, A. Koicheva, K.V. Bevziuk, K. Pluta, D. Snigur, Simultaneous determination of Sunset Yellow and Tartrazine in soft drinks on carbon-paste electrode modified by silica impregnated with cetylpyridinium chloride, J. Food Meas. Charact. 13 (2019) 1964–1972, https://doi.org/10.1007/s11694-019-00115-6.
[17] G.K. Jayaprakash, B.E.K. Swamy, S. Rajendrachari, S.C. Sharma, R. Flores-Morenoe, Dual descriptor analysis of cetylpyridinium modified carbon paste electrodes for ascorbic acid sensing applications, J. Mol. Liq. 334 (2021), https://doi.org/10.1016/j.molliq.2021.116348.
[18] N. Sakač, D. Madunić-Čačić, D. Marković, L. Hok, R. Vianello, B. Šarkanj, B. Đurin, K. Hajdek, B. Smoljan, S. Milardović, B. Matasović, M. Jozanović, Potentiometric surfactant sensor based on 1,3-dihexadecyl-1*H*-benzo[*d*] imidazol-3-ium for anionic surfactants in detergents and household care products, Molecules 26 (2021) 3627, https://doi.org/10.3390/molecules26123627.
[19] N. Sakač, D. Marković, B. Šarkanj, D. Madunić-Čačić, K. Hajdek, B. Smoljan, M. Jozanović, Direct potentiometric study of cationic and nonionic surfactants in disinfectants and personal care products by new surfactant sensor based on 1,3-dihexadecyl−1*H*-benzo[*d*]imidazole-3-ium, Molecules 26 (2021) 1366, https://doi.org/10.3390/molecules26051366.
[20] N. Sakač, D. Madunić-čačić, M. Karnaš, B. Đurin, I. Kovač, M. Jozanović, The influence of plasticizers on the response characteristics of the surfactant sensor for cationic surfactant determination in disinfectants and antiseptics, Sensors 21 (2021) 3535, https://doi.org/10.3390/s21103535.
[21] M. Jozanović, N. Sakač, M. Karnaš, M. Medvidović-Kosanović, Potentiometric sensors for the determination of anionic surfactants – a review, Critical Rev. Anal. Chem. 51 (2021) 115–137, https://doi.org/10.1080/10408347.2019.1684236.
[22] S. Petersen, S. Kaule, F. Stein, I. Minrath, K.-P. Schmitz, U. Kragl, K. Sternberg, Novel paclitaxel-coated angioplasty balloon catheter based on cetylpyridinium salicylate: Preparation, characterization and simulated use in an in vitro vessel model, Mater. Sci. Eng. C 33 (2013) 4244–4250, https://doi.org/10.1016/j.msec.2013.06.021.
[23] M. Fizer, M. Filep, O. Fizer, O. Fričová, R. Mariychuk, Cetylpyridinium picrate: Spectroscopy, conductivity and DFT investigation of the structure of a new ionic liquid, J. Mol. Struct. 1229 (2021), https://doi.org/10.1016/j.molstruc.2020.129803.
[24] E.W. Anacker, H.M. Ghose, Counterions and micelle size. II. Light scattering by solutions of cetylpyridinium salts, J. Am. Chem. Soc. 90 (1968) 3161–3166, https://doi.org/10.1021/ja01014a034.
[25] W. Selig, Comparison of various sensors in the potentiometric microdetermination of nitroform and perchlorate with cetylpyridinium chloride, Mikrochim Acta 79 (1983) 333–345, https://doi.org/10.1007/BF01204816.
[26] W.S. Selig, Sequential titrations of anions with cetylpyridinium chloride, Fresenius J. Anal. Chem. 330 (1988) 127–129, https://doi.org/10.1007/BF00470723.

[27] S.T. Goga, A.V. Lebed, N.O. Mchedlov-Petrossyan, Conductivity and dissociation constants of quaternary ammonium perchlorates and picrates in 4-methyl-pentan-2-one, J. Chem. Eng. Data 55 (2010) 1887–1892, https://doi.org/10.1021/je9008969.
[28] S.T. Goga, N.O. Mchedlov-Petrossyan, E.N. Glazkova, A.V. Lebed, Thermodynamics of solubility and solvation ofN-cetylpyridinium perchlorate and related compounds in water–propanol-2 system, J. Mol. Liq. 177 (2013) 237–242, https://doi.org/10.1016/j.molliq.2012.11.004.
[29] N.O. Mchedlov-Petrossyan, N.N. Kamneva, Y.T.M. Al-Shuuchi, A.I. Marynin, Interaction of C60aggregates with electrolytes in acetonitrile, Colloids Surf. A Physicochem. Eng. Asp. 516 (2017) 345–353, https://doi.org/10.1016/j.colsurfa.2016.12.035.
[30] T. Hatakeyama, Zh. Liu, Handbook of thermal analysis, Wiley, 1998, 471 p.
[31] J.-C. Zhao, Methods for Phase Diagram Determination, Elsevier Science, 2007.
[32] A. Altomare, C. Cuocci, C. Giacovazzo, A. Moliterni, R. Rizzi, N. Corriero, A. Falcicchio, EXPO2013: a kit of tools for phasing crystal structures from powder data, J. Appl. Crystallogr. 46 (2013) 1231–1235, https://doi.org/10.1107/S0021889813013113.
[33] A. Altomare, N. Corriero, C. Cuocci, A. Falcicchio, A. Moliterni, R. Rizzi, EXPO software for solving crystal structures by powder diffraction data: methods and application, Cryst. Res. Technol. 50 (2015) 737–742, https://doi.org/10.1002/crat.201500024.
[34] W. Kraus, G. Nolze, Powder cell – a program for the representation and manipulation of crystal structures and calculation of the resulting X-ray powder patterns, J. Appl. Crystallogr. 29 (1996) 301–303, https://doi.org/10.1107/S0021889895014920.
[35] M.D. Hanwell, D.E. Curtis, D.C. Lonie, T. Vandermeersch, E. Zurek, G.R. Hutchison, Avogadro: an advanced semantic chemical editor, visualization, and analysis platform, J. Cheminform. 4 (2012) 1–17, https://doi.org/10.1186/1758-2946-4-17.
[36] F. Neese, Software update: The ORCA program system – Version 5.0, Wiley Interdisc. Rev. Comput. Mol. Sci. 12 (2022), e1606, https://doi.org/10.1002/wcms.1606.
[37] F. Neese, F. Wennmohs, U. Becker, C. Riplinger, The ORCA quantum chemistry program package, J. Chem. Phys. 152 (2020), https://doi.org/10.1063/5.0004608.
[38] F. Neese, The SHARK integral generation and digestion system, J. Comput. Chem. (2022), https://doi.org/10.1002/jcc.26942.
[39] P. Pinski, F. Neese, Analytical gradient for the domain-based local pair natural orbital second order Møller-Plesset perturbation theory method (DLPNO-MP2), J. Chem. Phys. 150 (2019), https://doi.org/10.1063/1.5086544.
[40] R. Laplaza, F. Peccati, R.A. Boto, C. Quan, A. Carbone, J.-P. Piquemal, Y. Maday, J. Contreras-García, NCIPLOT and the analysis of noncovalent interactions using the reduced density gradient, Wiley Interdiscip. Rev. Comput. Mol. Sci. 11 (2020), https://doi.org/10.1002/wcms.1497.
[41] T.R. Wilson, A.N. Alexandrova, M.E. Eberhart, Electron density geometry and the quantum theory of atoms in molecules, J. Phys. Chem. A 125 (2021) 10622–10631, https://doi.org/10.1021/acs.jpca.1c09359.
[42] F.R. Wagner, V. Bezugly, M. Kohout, Y.u. Grin, Charge decomposition analysis of the electron localizability indicator: a bridge between the orbital and direct space representation of the chemical bond, Chem. Eur. J. 13 (2007) 5724–5741, https://doi.org/10.1002/chem.200700013.
[43] T. Lu, F. Chen, Multiwfn: a multifunctional wavefunction analyzer, J. Comput. Chem. 33 (2012) 580–592, https://doi.org/10.1002/jcc.22885.
[44] F. Teixeira, M.N.D.S. Cordeiro, Improving vibrational mode interpretation using bayesian regression, J. Chem. Theory Comput. 15 (2019) 456–470, https://doi.org/10.1021/acs.jctc.8b00439.
[45] A.R. Allouche, Gabedit e a graphical user interface for computational chemistry softwares, J. Comput. Chem. 32 (2011) 174–182, https://doi.org/10.1002/jcc.21600.
[46] W. Humphrey, A. Dalke, K. Schulten, VMD: visual molecular dynamics, J. Mol. Graph. 14 (1996) 33–38, https://doi.org/10.1016/0263-7855(96)00018-5.
[47] Y. Zhao, D.G. Truhlar, The M06 suite of density functionals for main group thermochemistry, thermochemical kinetics, noncovalent interactions, excited states, and transition elements: two new functionals and systematic testing of four M06-class functionals and 12 other functionals, Theor. Chem. Acc. 120 (2008) 215–241, https://doi.org/10.1007/s00214-007-0310-x.
[48] R. Jasiński, A new insight on the molecular mechanism of the reaction between (Z)-C, N-diphenylnitrone and 1,2-bismethylene-3,3,4,4,5,5-hexamethylcyclopentane, J. Mol. Graphics Model. 94 (2020), https://doi.org/10.1016/j.jmgm.2019.107461.
[49] G. Mlostoń, R. Jasiński, K. Kula, H. Heimgartner, A DFT study on the Barton-Kellogg reaction – the molecular mechanism of the formation of thiiranes in the reaction between diphenyldiazomethane and diaryl thioketones, Eur. J. Organic Chem. 2020 (2020) 176–182, https://doi.org/10.1002/ejoc.201901443.
[50] A. Kącka-Zych, R. Jasiński, Unexpected molecular mechanism of trimethylsilyl bromide elimination from 2-(trimethylsilyloxy)-3-bromo-3-methyl-isoxazolidines, Theor. Chem. Accounts 138 (2019) 81, https://doi.org/10.1007/s00214-019-2467-5.
[51] K.J. Coverta, A. Bodi, K.G. Torma, K. Voronova, T. Baer, B. Sztáray, To roam or not to roam, that is the question for the methyl group in isopropanol cations, Int. J. Mass Spectrometry 459 (2021), https://doi.org/10.1016/j.ijms.2020.116469.
[52] A. Kącka-Zych, R. Jasiński, A DFT study on the molecular mechanism of the conjugated nitroalkenes polymerization process initiated by selected unsaturated nucleophiles, Theor. Chem. Accounts 139 (2020) 119, https://doi.org/10.1007/s00214-020-02627-7.
[53] N. Mardirossian, M. Head-Gordon, How accurate are the Minnesota density functionals for noncovalent interactions, isomerization energies, thermochemistry, and barrier heights involving molecules composed of main-group elements?, J Chem. Theory Comput. 12 (2016) 4303–4325, https://doi.org/10.1021/acs.jctc.6b00637.
[54] M. Walker, A.J.A. Harvey, A. Sen, C.E.H. Dessent, Performance of M06, M06–2X, and M06-HF density functionals for conformationally flexible anionic clusters: M06 functionals perform better than B3LYP for a model system with dispersion and ionic hydrogen-bonding interactions, J. Phys. Chem. A 117 (2013) 12590–12600, https://doi.org/10.1021/jp408166m.
[55] J.G. Brandenburg, C. Bannwarth, A. Hansen, S. Grimme, B97–3c: A revised low-cost variant of the B97-D density functional method, J. Chem. Phys. 148 (2018), https://doi.org/10.1063/1.5012601.
[56] Z. Sun, Z. Gong, L. Zheng, P. Kalhor, Z. Huaid, Z. Liu, Molecular modelling of ionic liquids: general guidelines on fixed-charge force fields for balanced descriptions, Journal of Ionic Liquids 2 (2022), https://doi.org/10.1016/j.jil.2022.100043.
[57] E. Perlt, P. Ray, A. Hansen, F. Malberg, S. Grimme, B. Kirchner, Finding the best density functional approximation to describe interaction energies and structures of ionic liquids in molecular dynamics studies, J. Chem. Phys. 148 (2018), https://doi.org/10.1063/1.5013122.
[58] M. Garcia-Ratés, F. Neese, Effect of the solute cavity on the solvation energy and its derivatives within the framework of the Gaussian charge scheme, J. Comput. Chem. 41 (2020) 922–939, https://doi.org/10.1002/jcc.26139.
[59] M. Garcia-Ratés, F. Neese, Efficient implementation of the analytical second derivatives of Hartree-Fock and hybrid DFT energies within the framework of the conductor-like polarizable continuum model, J. Comput. Chem. 40 (2020) 1816–1828, https://doi.org/10.1002/jcc.25833.
[60] C.J. Schattenberg, M. Kaupp, Extended benchmark set of main-group nuclear shielding constants and NMR chemical shifts and its use to evaluate modern DFT methods, J. Chem. Theory Comput. 17 (2021) 7602–7621, https://doi.org/10.1021/acs.jctc.1c00919.
[61] M. Fizer, M. Slivka, N. Korol, O. Fizer, Identifying and explaining the regioselectivity of alkylation of 1,2,4-triazole-3-thiones using NMR, GIAO and DFT methods, J. Mol. Struct. 1223 (2021), https://doi.org/10.1016/j.molstruc.2020.128973.
[62] G.L. Stoychev, A.A. Auer, J. Gauss, F. Neese, DLPNO-MP2 second derivatives for the computation of polarizabilities and NMR shieldings, J. Chem. Phys. 154 (2021), https://doi.org/10.1063/5.0047125.
[63] F. Jensen, Segmented contracted basis sets optimized for nuclear magnetic shielding, J. Chem. Theory Comput. 11 (2015) 132–138, https://doi.org/10.1021/ct5009526.
[64] D.J. Devlin, P.J. Herley, Thermal decomposition and dehydration of sodium perchlorate monohydrate, Reactivity of Solids 3 (1987) 75–84, https://doi.org/10.1016/0168-7336(87)80019-0.
[65] P.J. Haines, Thermal methods of analysis principles, applications and problems. Springer Netherlands (1995) 286 p.
[66] D.G. Archer, S. Rudtsch, Enthalpy of fusion of indium: a certified reference material for differential scanning calorimetry, J. Chem. Eng. Data 48 (2003) 1157–1163, https://doi.org/10.1021/je030112g.
[67] V. Bertolasi, P. Gilli, G. Gilli, Hydrogen bonding and electron donor-acceptor (EDA) interactions controlling the crystal packing of picric acid and its adducts with nitrogen bases. Their rationalization in terms of the pka equalization and electron-pair saturation concepts, Cryst. Growth Des. 11 (2011) 2724–2735, https://doi.org/10.1021/cg101007a.
[68] G.-L. Zhang, Y.-T. Li, Z.Y. Wu, Y.-L. Song, Sodium perchlorate in the space group Pnma, Acta Crystallogr. E: Crystallogr. Commun. 62 (2006) i150–i151, https://doi.org/10.1107/S1600536806022975.
[69] A.D. Becke, Density-functional thermochemistry. III. The role of exact exchange, J. Chem. Phys. 98 (1993) 5648–5652, https://doi.org/10.1063/1.464913.
[70] K.A. Guzzetti, M.A. Iramain, R.A. Rudyk, M.E. Manzur, S.A. Brandan, Vibrational studies of species derived from potent S(+) and R(-) ecstasy stimulant by using ab-initio calculations and the SQM approach, Biointerface Res. Appl. Chem. 10 (2020) 6783–6809, https://doi.org/10.33263/BRIAC106.67836809.
[71] J.R. Hidalgo, S.A. Brandán, Structural study and vibrational assignments of anticonvulsant topiramate by using DFT calculations and two harmonic force fields, Biointerface Res. Appl. Chem. 11 (2021) 9880–9903, https://doi.org/10.33263/BRIAC113.98809903.
[72] A. Sagaama, O. Noureddine, S.A. Brandán, A. Jarczyk-Jędryka, H.T. Flakus, H. Ghalla, N. Issaoui, Molecular docking studies, structural and spectroscopic properties of monomeric and dimeric species of benzofuran-carboxylic acids derivatives: DFT calculations and biological activities, Comput. Biol. Chem. 87 (2020), https://doi.org/10.1016/j.compbiolchem.2020.107311.
[73] K. Karrouchi, S.A. Brandán, Y. Sert, M. El Karbane, S. Radi, M. Ferbinteanu, Y. Garcia, M. Ansar, Synthesis, structural, molecular docking and spectroscopic studies of (E)-N'-(4-methoxybenzylidene)-5-methyl-1H-pyrazole-3-carbohydrazide, J. Mol. Struct. 1225 (2021), https://doi.org/10.1016/j.molstruc.2020.129072.
[74] Z. Vitková, J. Oremusová, P. Herdová, O. Ivánková, A. Vitko, Association, distribution, liberation, and rheological balances of alkyldimethylbenzylammonium chlorides (C12–C16), Molecules 22 (2017) 1802, https://doi.org/10.3390/molecules22101802.

[75] M. Fizer, O. Fizer, Theoretical study on charge distribution in cetylpyridinium cationic surfactant, J. Mol. Model. 27 (2021) 203, https://doi.org/10.1007/s00894-021-04820-2.
[76] C.F. Matta, O. Lombardi, J.J. Arriaga, Two-step emergence: the quantum theory of atoms in molecules as a bridge between quantum mechanics and molecular chemistry, Found. Chem. 22 (2020) 107–129, https://doi.org/10.1007/s10698-020-09352-w.
[77] M. Medimagh, N. Issaoui, S. Gatfaoui, S.A. Brandán, O. Al-Dossary, H. Marouani, M.J. Wojcik, Impact of non-covalent interactions on FT-IR spectrum and properties of 4-methylbenzylammonium nitrate. A DFT and molecular docking study, Heliyon 7 (2021), https://doi.org/10.1016/j.heliyon.2021.e08204.